RSC Advances

PAPER

View Article Online
View Journal | View Issue

Cite this: *RSC Adv.*, 2022, **12**, 939

Porous carbon-confined Co_xS_y nanoparticles derived from ZIF-67 for boosting lithium-ion storage†

Xiao Su,[a] Wen Li,*[a] Haining Sun,[b] Jian Wang,*[b] Sisi Hu,[a] Fei Yuan,[a] Di Zhang[a] and Bo Wang*[a]

Reasonable regulation and synthesis of hollow nanostructure materials can provide a promising electrode material for lithium-ion batteries (LIBs). In this work, utilizing a metal–organic framework (MOF, ZIF-67) as the raw material and template, a composite of Co_xS_y with a carbon shell is successfully formed through a hydrothermal vulcanization and a subsequent high temperature sintering process. The as-obtained Co_xS_y(700) material sintered at 700 °C has a large specific surface area, and at the same time possesses a hollow carbon shell structure. Benefiting from unique structural advantages, the volume change during the electrochemical reaction can be well alleviated, and thus the structural stability is greatly improved. The presence of the carbon matrix can also offer sufficient ion/electron transfer channels, contributing to the enhanced electrochemical performance. As a result, the Co_xS_y(700) electrode can deliver an excellent capacity of 875.6 mA h g^{-1} at a current density of 100 mA g^{-1}. Additionally, a high-capacity retention of 88% is achieved after 1000 cycles when the current density is increased to 500 mA g^{-1}, and exhibiting a prominent rate capability of 526.5 mA h g^{-1}, simultaneously. The novel synthesis route and considerable electrochemical properties presented by this study can afford guidance for the exploration of high-performance cobalt sulfide anodes in LIBs.

Received 23rd November 2021
Accepted 9th December 2021

DOI: 10.1039/d1ra08581f

rsc.li/rsc-advances

1. Introduction

Lithium-ion batteries (LIBs), as a new type of energy storage device, have been widely used for secondary energy storage in various portable electronic devices, and have promoted the development of new energy electric vehicles, energy conservation and environmental protection, as well as other emerging industries.[1–4] However, the main anode material for current commercial LIBs is graphite, and its theoretical capacity is only 372 mA h g^{-1}, which cannot meet the needs of high energy density and long cycle lifespan for further large-scale applications.[5–7] Therefore, it is necessary and urgent to find high-performance electrode materials with high-capacity, favorable cyclability and so on for LIBs to compensate the disadvantages of current electrode materials.[8–11]

Transition metal sulfides (TMSs) are considered as one of the most promising anode materials for lithium-ion batteries because they not only have a high specific capacity, but also generally exhibit good electrical conductivity, and excellent mechanical and thermal stability.[12] Among them, cobalt sulfides (Co_xS_y) with excellent electrochemical activity and high theoretical capacity (>400 mA h g^{-1}), as a subset of transition metal sulfides, have been extensively investigated in lithium-ion battery anodes.[13,14] Unfortunately, the huge volume change caused by the insertion/extraction process of bulky Li-ions will inevitably induce structure fracture of the Co_xS_y electrode, thus exhibiting a poor cycling stability.[12] At present, many efforts have been made to remove these obstacles. For example, constructing nanostructures of Co_xS_y particles can significantly reduce the diffusion pathway of ions and increase the contact area between the electrode and electrolyte, which is conducive to improving the reaction kinetics.[15] Besides, integrating Co_xS_y active material and a carbon buffer matrix can not only effectively improve the conductivity of the composite electrode, but also well maintain its structural integrity against deformation upon cycling, thereby enhancing the rate capacity and cycling stability.[16,17] In addition, rationally designed hollow porous structures can generate numerous active sites for lithium storage, and in addition the large specific surface area induced by the porous structure can also provide fast channels for ion/electron transfer, thus enabling superior electrochemical performance.[18,19]

As is well known, metal organic frameworks (MOFs) with a unique and uniform morphological structure can provide

[a]Hebei Key Laboratory of Flexible Functional Materials, School of Materials Science and Engineering, Hebei University of Science and Technology, Shijiazhuang 050000, China. E-mail: liwen_cc@yeah.net; wangbo1996@gmail.com

[b]Innovation Center for Hebei Intelligent Grid Distribution Technology, Shijiazhuang Kelin Electric Co., Ltd, Shijiazhuang 050000, China. E-mail: wangjian0534@sina.com

† Electronic supplementary information (ESI) available. See DOI: 10.1039/d1ra08581f

a huge opportunity for the preparation of hollow structure materials when they act as a template or precursor.[20,21] Therefore, exploring the application of MOF-based derived materials in electrochemical energy storage has attracted more and more attention. Zeolite imidazole salt frameworks (ZIFs) are typical MOF materials, in which ZIF-67 is usually recognized as an effective precursor or template for constructing porous and hollow structured materials, due to its good adjustable physical and chemical properties, typical nano-particle size, large surface area and effective mass transfer.[22] Previous studies have shown that ZIF-67-derived cobalt sulfide can effectively alleviate structural changes caused by stress, attributed to the rich cavities that it generates. Also, the porous thin walls can expose more electrochemically active sites to allow full penetration of the electrolyte and rapid ion transfer, thereby ensuring an excellent electrochemical performance.[23,24]

In view of the above mentioned, combining the individual merits of nano-size, hollow structure, and a carbon buffer matrix in one anode material is attractive. Herein, a composite (Co_xS_y(700)) of a hollow Co_xS_y nanomaterial and carbon skeleton is synthesized by utilizing ZIF-67 as a precursor. The resulting Co_xS_y(700) is expected to offer facile Li-ion kinetics, fast electron conductive pathways and robust structural stability. When Co_xS_y(700) is applied as an anode for LIBs, it displays a satisfactory reversible capacity of 875.6 mA h g^{-1} at 100 mA g^{-1}, and an outstanding cycling lifetime over 1000 cycles is also achieved at 500 mA g^{-1}. More importantly, as a good candidate for the anode, Co_xS_y(700) demonstrates a facile design strategy to construct the electrode material in LIBs.

2. Experimental

2.1. Material synthesis

2.1.1. Preparation of the ZIF-67 templates. The ZIF-67 templates were prepared by following a method reported in the literature.[25] First, cobalt nitrate hexahydrate was dissolved in methanol to form a solution (0.1 M). 2-Methylimidazole was dissolved in methanol to generate another clear solution (1.2 M). Then, the two solutions were mixed uniformly under vigorous stirring. Then, the uniformly mixed solution was allowed to stand at room temperature for 12 hours until the solid powder settled. After that, the resulting blue precipitate was collected, washed with methanol several times, and then dried at 80 °C for 24 hours. The blue precipitate obtained was the ZIF-67 template.

2.1.2. Preparation of the ZIF-67(m). The obtained ZIF-67 blue powder was sintered in a flowing argon atmosphere at 500 °C, 600 °C, and 700 °C for 3 hours to obtain a Co/C composite electrode material called ZIF-67(m), where m represents the sintering temperature (m = 500 represents 500 °C, m = 600 represents 600 °C, m = 700 represents 700 °C).

2.1.3. Preparation of the hollow Co_xS_y(n). The above-mentioned ZIF-67 blue particles (25 mg) were redispersed in 6 mL of ethanol under ultrasonic treatment for 30 min to obtain a homogeneous solution. Then, 2 mL of thioacetamide (0.1875 mM, ethanol) was added to the above solution under continuous stirring, and it was kept hydrothermally at 90 °C for 1 h. After being naturally cooled to room temperature, the black precipitated powder was collected by centrifugal washing with ethanol and deionized water, and then the powder was dried at 60 °C for 24 hours. The black powder obtained was hollow Co_xS_y.

The hollow Co_xS_y powder was sintered at 600 °C, 700 °C and 800 °C for 3 hours in a full argon atmosphere to obtain a Co_xS_y/C composite electrode material named hollow Co_xS_y(n), where n represents the sintering temperature (n = 600 represents 600 °C, n = 700 represents 700 °C, n = 800 represents 800 °C).

2.1.4. Preparation of the hollow Co_xS_y(700) without carbon. After the as-prepared Co_xS_y(700) was further annealed at 300 °C for 0.5 h in air with a heating rate of 10 °C min^{-1}, the hollow Co_xS_y(700) without carbon could be obtained (marked as Co_xS_y(700)-WC). According to a previous report, the carbon in Co_xS_y(700) could be completely removed at 300 °C in air.[24]

2.2. Characterization

The crystal structure was determined by X-ray diffraction (XRD, X Pert Powder, Holland) with Cu Kα radiation (λ = 1.5418 Å). X-ray photoelectron spectroscopy (XPS, Quantera II, PHI, America) was used to measure the surface chemical states. The chemistry information was examined by energy-dispersive X-ray spectroscopy (EDS, attachments of JEOL JEM-2010). The specific surface area was measured using the nitrogen adsorption–desorption technique (BET, SSA-4300, Bjbuilder, China). The microstructure was observed on a scanning electron microscope (SEM, Gemini SEM300-71-31, ZEISS, Germany) and transmission electron microscope (TEM, JEM-2100, JEOL, Japan). Thermogravimetric analysis (TGA, Labsys NETZSCH TG-209) was used to investigate the thermal stability of the ZIF-67.

2.3. Electrochemical characterization

The electrochemical test was performed using a standard CR2032 coin cell. The working electrode was prepared by mixing 80 wt% of active material, 10 wt% of polyvinylidene fluoride (PVDF) in *N*-methylpyrrolidone (NMP) and 10 wt% of conductive Super-P, and then adhering it onto a Cu foil current collector. After that, the electrode was dried under vacuum at 80 °C for 12 h. The active material mass loading of each electrode was about 1.1–1.3 mg cm^{-2}. Lithium foil was used as the anode, a polypropylene membrane (Celgard 2400, America) was used as a separator and 1.0 M $LiPF_6$ in EC : DMC = 1 : 1 wt% (LB-064, Dodochem, China) was used as an electrolyte. The assembly process of the test cell was carried out in an argon-filled glove box. The galvanostatic discharge–charge test was carried out using a battery tester (LAND, CT2001A, Wuhan, China) at different current densities from 0 to 3 V (*vs.* Li^+/Li). Cyclic voltammetry (CV) (voltage range: 0–3 V, scan rate: 0.1 mV s^{-1}) and electrochemical impedance spectroscopy (EIS) (frequency range: 100 kHz–0.01 Hz) tests were performed on an electrochemical workstation (CHI660E, Shanghai, China).

3. Results and discussion

The synthesis routes of ZIF-67(m) and Co_xS_y(n) are shown in Fig. 1. First, the ZIF-67 precursor was fabricated by a simple solution precipitation method at room temperature. The as-obtained ZIF-67 was directly calcinated at a high temperature to prepare ZIF-67(m). Subsequently, the hollow Co_xS_y(n) was synthesized by hydrothermal vulcanization of ZIF-67, followed by a carbonization process in Ar flow for 3 h. Furthermore, as observed in Fig. S1,† the Co_xS_y powder experiences a severe weight loss at ~500–600 °C, which is caused by the collapse of the MOF skeleton and decomposition of the organic ligand.[22] The total weight loss from room temperature to 800 °C is 36.2 wt%. Therefore, several different Co_xS_y/C composites were obtained by calcining the Co_xS_y powder at 600, 700, and 800 °C in an Ar atmosphere.

X-ray powder diffraction (XRD) was performed to verify the composition and structure evolution of the obtained products. For ZIF-67 (Fig. S2a†), it can be clearly seen that the peaks of the starting seeds matched well with the patterns of simulated Co-based ZIF-67, which corresponds with the previous reported MOFs (JCPDS 33-0448).[26] After high temperature carbonization, the diffraction peaks of Co (JCPDS 88-2325) and C (JCPDS 75-1621) are obviously observed in Fig. S2b.† This result indicates that the organic components present in the metal–organic framework material are successfully pyrolyzed to form carbon element during the carbonization process, and cobalt metal ions can be thermally reduced to metallic Co by carbon at this stage.[27] In addition, the diffraction peaks of the ZIF-67(600) phase are strong and sharp, indicating that an overall crystallization has occurred. As shown in Fig. 2, the Co_9S_8 and Co_4S_3 can be detected through the XRD pattern of Co_xS_y(700), corresponding to JCPDS card number 73-1442 and 73-1703, respectively. In particular, the Co_9S_8 and Co_4S_3 are confirmed as belonging to the $Fm\bar{3}m$(225) and $Fd\bar{3}m$(227) space group, respectively.[28,29] Therefore, it can be determined that cobalt–sulfur compounds are formed after the vulcanization modification and subsequent carbonization process. As a result, the obtained cobalt–sulfur compounds will increase the storage capacity of lithium.

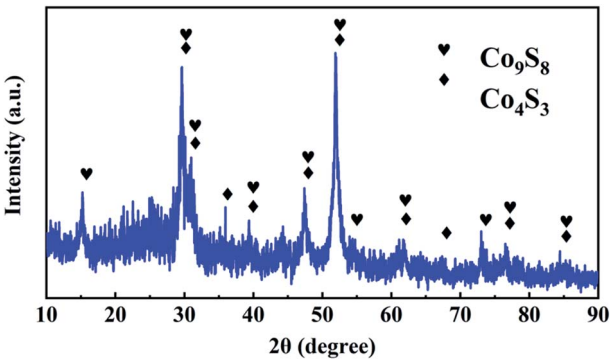

Fig. 2 XRD patterns of Co_xS_y(700).

The XPS spectrum was obtained to further confirm the chemical composition and bonding information of the obtained products. As depicted in Fig. S3,† all of the samples are composed of C, O, N, S, and Co elements. Concretely, the detected O element can be ascribed to a small amount of oxidation in the test, and the N element resulted from the decomposition of the carbon source. The C 1s spectrum of Co_xS_y(700) can be divided into three peaks, which correspond to C–C (284.8 eV), C–N (286.0 eV) and C=O (288.25 eV), respectively. The C 1s spectrum in Co_xS_y(700) (Fig. 3a) is deconvoluted into three spectral peaks, namely, C–C (284.8 eV), C–N (286.05 eV) and C=O (288.52 eV),[16,20] respectively, indicating that C element still exists in the final material Co_xS_y(700). Moreover, the Co 2p spectrum of Co_xS_y(700) in Fig. 3b presents a Co^{3+} peak (794.21 eV/778.34 eV) in addition to the Co^{2+} (795.93 eV/780.44 eV) and sat. peaks (803.72 eV/783.12 eV).[8,22] It is worth mentioning that the S 2p spectrum (Fig. 3c) is assigned as

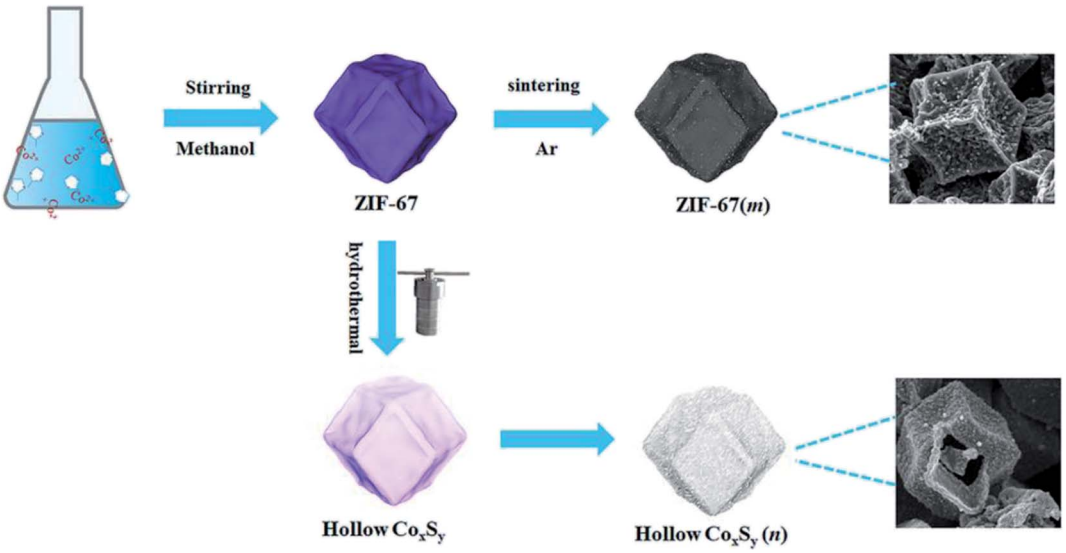

Fig. 1 Schematic illustration of the synthesis of ZIF-67(m) and hollow Co_xS_y(n).

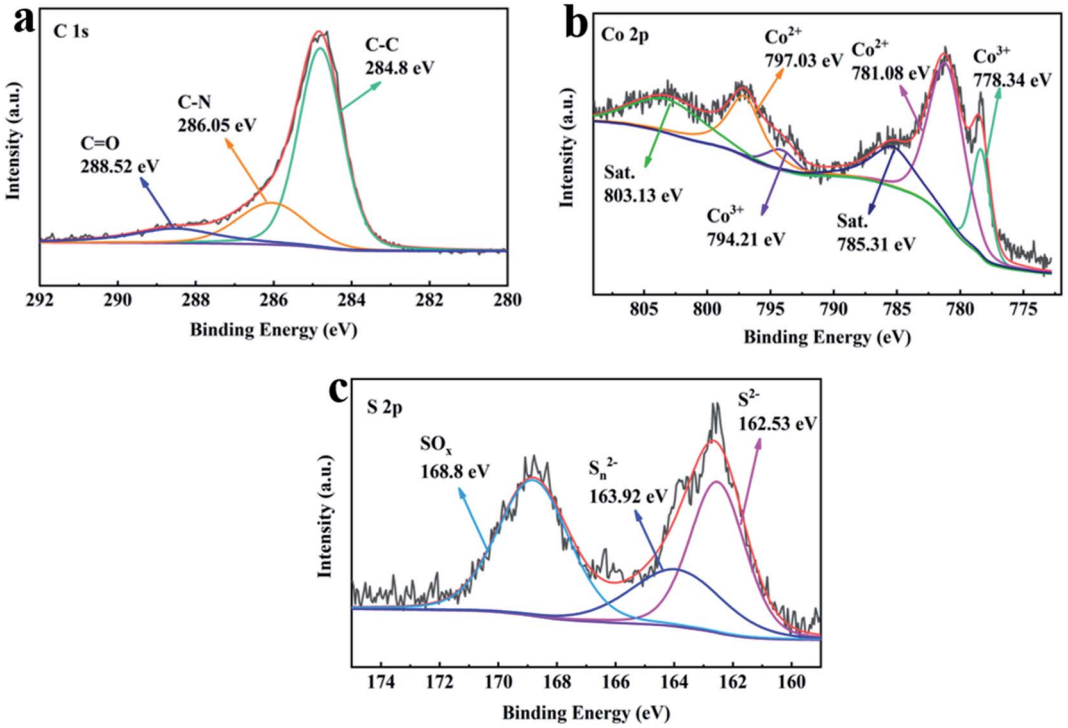

Fig. 3 XPS spectra of C 1s (a), Co 2p (b) and S 2p (c) for Co_xS_y(700).

S^{2-} (162.53 eV) and S_n^{2-} (163.92 eV), indicating the successful preparation of cobalt–sulfur compounds.[8,14,30]

In addition, SEM and TEM were used to observe the morphological structure of the prepared materials. The topography of the ZIF-67 template is shown in Fig. S4a–c;† the ZIF-67 precursor presents a uniform dodecahedron structure, and its diameter is approximately 200–300 nm (Fig. S4a and b†). The TEM image (Fig. S4c†) exhibits a smooth surface with a thickness of 5–10 nm; this structural feature is favorable for forming a uniform and stable carbon shell during the high temperature annealing process. After hydrothermal vulcanization, the formed Co_xS_y also exhibits a dodecahedron shape, and the particle size is similar to that of the ZIF-67 precursor (Fig. S4d–f†). Different from the solid structure of ZIF-67, the Co_xS_y displays a hollow nanocage architecture, and simultaneously possesses an obvious shell wall with a thickness of about 5 nm. After sintering at a high temperature of 600–800 °C, the hollow nanocage structure is maintained well (as shown in Fig. 4a–f). However, compared to Co_xS_y(700), the distribution of Co_xS_y(600) and Co_xS_y(800) is slightly uneven along with some aggregation. The lattice spacings of 0.28 nm and 0.18 nm are found in Co_xS_y(700) (Fig. 4h), corresponding to the (440) crystal plane of Co_9S_8 and the (311) crystal plane of Co_4S_3,[31–33] respectively. The energy dispersive X-ray (EDS) spectrum of Co_xS_y(700) is shown in Fig. 4i and j, where the uniform distribution of Co, C, and S elements further confirms the reliability of the hybrid nanostructure. Importantly, the successful introduction of carbon matrix can improve the conductivity and maintain the structural integrity, contributing to boosting the electrochemical performance of the Co_xS_y(700) anode in LIBs. Through the Brunauer Emmett Teller (BET) measurements (Fig. S5†), it can be discovered that the specific surface area of Co_xS_y(700) is 338.2224 $m^2\ g^{-1}$. The achievement of a high specific surface area is closely related to the hollow structure of the Co_xS_y(700) material, and the improved specific surface area can promote rapid infiltration of electrolyte and shorten the diffusion path, resulting in good properties for fast charging/discharging.[34]

The electrochemical properties of Co_xS_y(600), Co_xS_y(700), and Co_xS_y(800) were systematically studied in a coin-type half-cell. The cyclic voltammetry (CV) curves of Co_xS_y(700) at a potential of 0.01–3.0 V for the first three cycles are shown in Fig. 5a. In the initial cathodic scan, the peaks that appear at 0.15 V and 0.9 V are attributed to the intercalation of Li-ions and the formation of Li_xS and Co, respectively. Noticeably, the obvious cathodic peak at 0.65 V occurring in the first cycle and disappearing in the following cycles corresponds to the formation of a solid electrolyte (SEI) film and the decomposition of the electrolyte.[35,36] In the first anodic scan, oxidation peaks at about 0.6 V and 2.0 V can be clearly observed, corresponding to the deintercalation of Li-ions and the oxidation of metallic Co into Co_xS_y, respectively.[37] In addition, the subsequent cycle curves overlap well, signifying the considerable electrochemical reversibility in the Co_xS_y(700) electrode. The galvanostatic charge–discharge curves of Co_xS_y(700) at different current densities are shown in Fig. 5b. There is no doubt that the capacities decrease with an increase in current density, and this phenomenon can be well displayed by the rate tests (Fig. 5c). Concretely, the Co_xS_y(700) electrode exhibits the best rate capacity at each current density in comparison with Co_xS_y(600) and Co_xS_y(800). For Co_xS_y(700), the average charging specific capacities are 875.6, 797.1, 715.5, 576.1 and 405.9 mA h g^{-1} at 100, 200, 500, 1000 and 2000 mA g^{-1}, respectively. In addition,

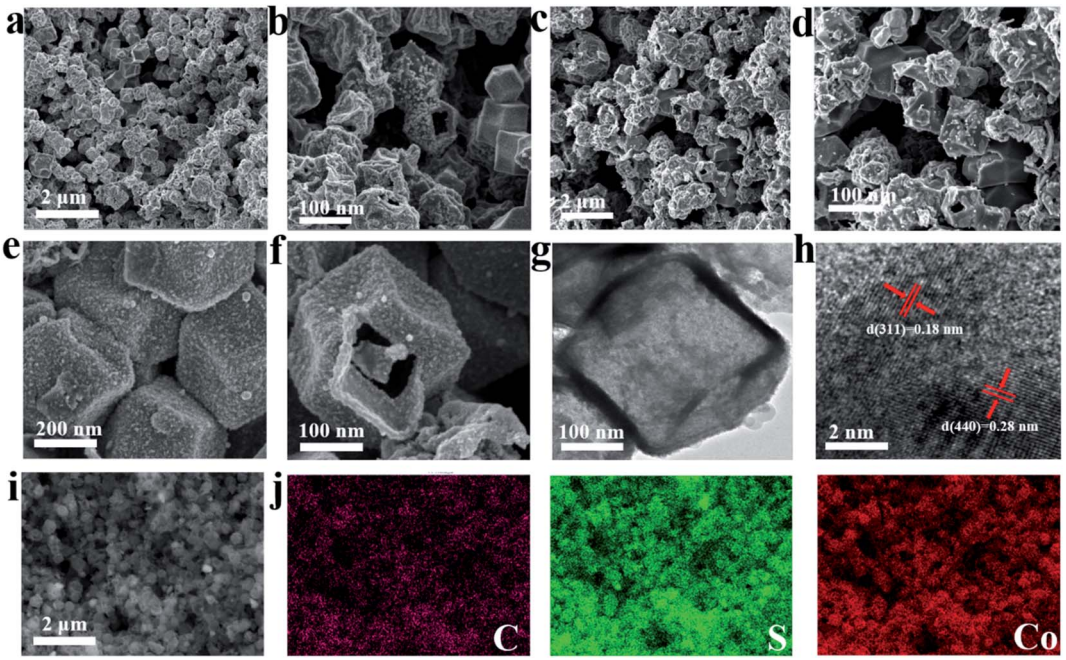

Fig. 4 SEM images of Co_xS_y(600) (a and b), Co_xS_y(800) (c and d), and Co_xS_y(700) (e and f). TEM images of Co_xS_y(700) (g and h). EDX mapping of Co_xS_y(700) (i and j).

when the current density finally returns to 100 mA g^{-1}, the charging specific capacity recovers to 885.9 mA h g^{-1}, indicating super reversibility and excellent rate properties. The reason for the increase in capacity can be mainly attributed to the fact that more electrolyte gradually enters the porous structure of the material during the charging and discharging process, the reaction sites are in contact with each other, and the electrode is activated.[38] For the Co_xS_y(600) and Co_xS_y(800) electrodes, their poor rate capability may be attributed to the uneven morphology and obvious agglomeration. A cycle capacity of about 468.4 mA h g^{-1} at 1 A g^{-1} was successfully achieved by the Co_xS_y(700) material (Fig. 5d), and a long-cycle lifespan over 1000 cycles with a retention rate of 88% was reached even though the test conditions were at a low current density of 500 mA g^{-1} (Fig. 5e). Besides, electrochemical impedance spectroscopy (EIS) (Fig. S6†) tests reveal that the Co_xS_y(700) exhibits a slight resistance change after 100 cycles at 1 A g^{-1}, indicating excellent reaction kinetics.

Moreover, we also investigated the morphology and electrochemical performance of the obtained ZIF-67(600). As observed in Fig. S7a and b,† ZIF-67(600) well maintains a uniform dodecahedron particle shape, size and structure. Obviously, many small particles on the ZIF-67(600) surface are clearly observed, and this phenomenon can be explained by the appearance of Co particles generated by thermal reduction.[30] It can be seen from the TEM image in Fig. S7c† that ZIF-67(600) is still a solid particle, and the enlarged TEM image shows that the lattice fringes of the nanoparticles are at 0.34 nm and 0.25 nm (Fig. S7d†), corresponding to the (002) crystal plane distance of graphite and the (111) crystal plane distance of Co, respectively. This result agrees well with the XRD analysis (Fig. 2b), and once again confirms the generation of Co and C in ZIF-67(600). As shown in Fig. S8a,† the CV curve of ZIF-67(600) was a typical curve of a carbon anode material; in the first discharge cycle, two peaks beginning at 1.5 and 0.65 V were clearly seen. The former was due to the irreversible reaction between Li-ions and carbon functional groups,[39] and the latter corresponds to the generation of an SEI membrane on the active material surface of the active electrode. In addition, there was a reduction peak near 1.2 V, which may be due to the side-reaction of the present Co and lithium.[40] The oxidation peak that appeared in the first cycle is in accordance with the previous literature reports.[40,41] From Fig. S8b and c,† the ZIF-67(600) anode obviously exhibits good rate performance and superior reversibility, especially compared to the ZIF-67(500) and ZIF-67(700) electrodes. As far as cycle life is concerned, the ZIF-67(600) can maintain a satisfactory capacity of 400.8 mA h g^{-1} at 1 A g^{-1} for 100 cycles (Fig. S8d†) and 294.8 mA h g^{-1} at 500 mA g^{-1} for 800 cycles (Fig. S8e†). However, when the current density is increased to 2 A g^{-1} (Fig. S8f†), the cycling capability of the ZIF-67(600) electrode is much lower than that of the Co_xS_y(700) electrode, which intuitively indicates the robust structure in Co_xS_y(700). However, the rate capability, cycling stability and capacity offered by the ZIF-67(600) active material are lower than those of the Co_xS_y(700). This further proves that the hydrothermal vulcanization strategy can improve the electrochemical performance of the electrode material. More importantly, we also synthesized hollow Co_xS_y(700) without carbon (marked as Co_xS_y(700)-WC), and unveiled its electrochemical performance in LIBs. As shown in Fig. S9a,† it can be clearly seen that Co_xS_y(700)-WC has lower rate capability at each current density than Co_xS_y(700), which is ascribed to the inferior conductivity of the Co_xS_y(700)-WC electrode resulting from the lack of carbon matrix. In terms of cycling performance, the Co_xS_y(700)-WC

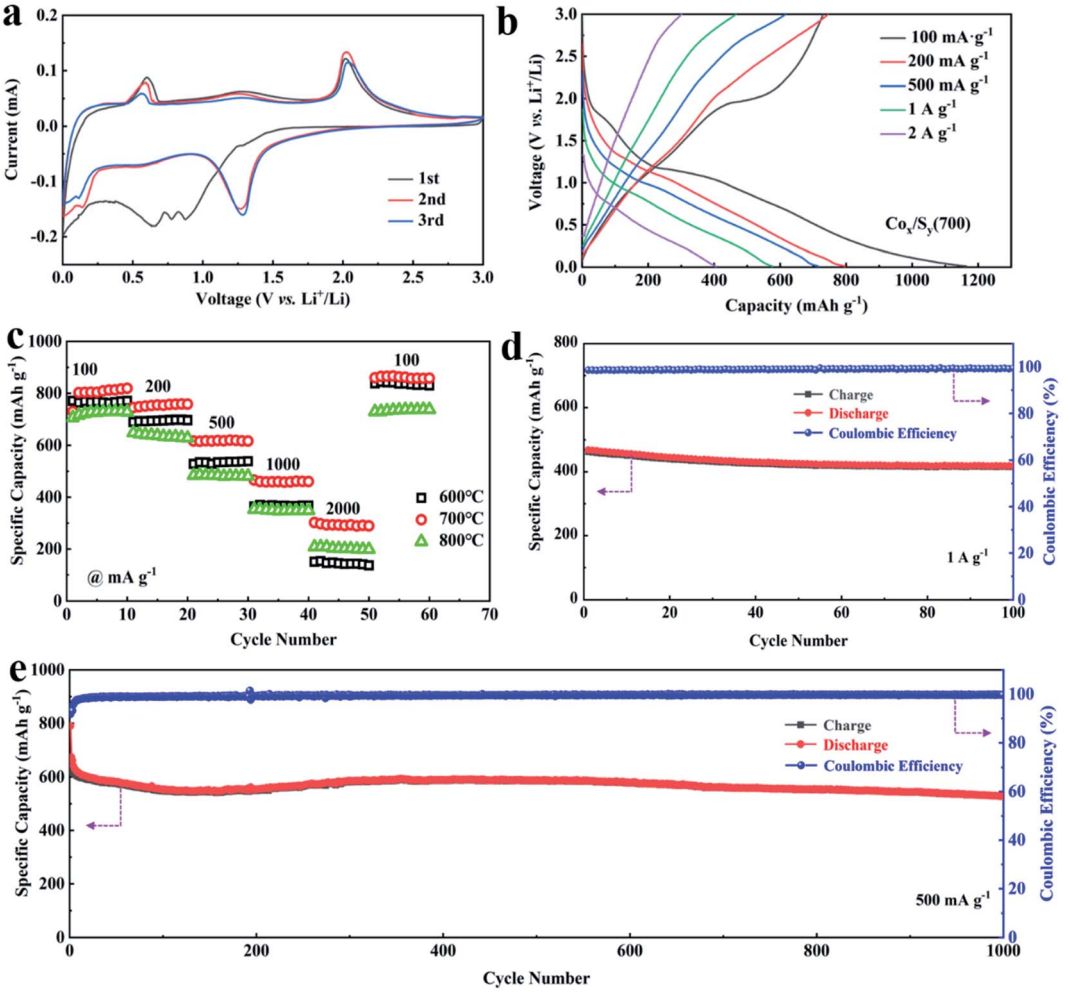

Fig. 5 CV curve (a) and galvanostatic charge–discharge curves at different rates (b) of Co_xS_y(700). Rate performance (c) of Co_xS_y(*n*); cycling stability at 1 A g^{-1} (d) and 0.5 A g^{-1} (e) of Co_xS_y(700).

electrode exhibits an obvious capacity fading during cycling (Fig. S9b†), and its capacity is only 151.9 mA h g^{-1} at 2 A g^{-1} for 700 cycles (Fig. S9c†), which is substantially lower than that of the Co_xS_y(700) electrode under the same conditions. This is mainly because the huge volume change induced by repeated Li-ion intercalation/deintercalation into/from Co_xS_y(700)-WC is not well alleviated. These results comprehensively suggest that the incorporation of the carbon matrix into Co_xS_y is of vital importance for improving the conductivity and alleviating the structure fluctuations, agreeing well with the analysis mentioned above.

4. Conclusion

In summary, using a ZIF-67 template as a precursor, we have successfully synthesized Co_xS_y(700) *via* hydrothermal vulcanization and carbonization, in which a nanostructure, hollow structure and porous carbon buffer matrix are combined into one material. The nanoscale level of the active material can effectively reduce the ion diffusion path, leading to enhanced reaction kinetics of lithium storage. In addition, the hollow structure can provide enough space to alleviate the volume change upon cycling, thus ensuring robust structural stability. The presence of porous carbon not only suppresses the structure deformation of the Co_xS_y particles, but also increases the electron conductivity. Benefiting from the synergistic effect of the above advantages, the Co_xS_y(700) electrode presents superior electrochemical performance, including rate capacity and cycling stability. Therefore, this work is expected to provide a reference for exploring cobalt sulfide anodes for high-performance LIBs.

Conflicts of interest

There are no conflicts to declare.

Acknowledgements

This work was supported by the National Natural Science Foundation of China (22008053, 52002111), the Key Research and Development Program of Hebei Province (20310601D, 205A4401D), the Natural Science Foundation of Hebei Province

(B2021208061), the High Level Talents Funding of Hebei Province (A202005006), and the Science Foundation of the University of Hebei Province (BJ2020026, BJ2021001).

References

1 W. Lei, L. Zhu, W. Zhang, G. Ding, G. Yang, L. Xie and X. Cao, Revealing the unique process of alloying reaction in Ni-Co-Sb/C nanosphere anode for high-performance lithium storage, *J. Colloid Interface Sci.*, 2021, **586**, 730–740.

2 B. Wang, F. Yuan, W. Wang, D. Zhang, H. Sun, K. Xi, D. Wang, J. Chu, Q. Wang and W. Li, A carbon microtube array with a multihole cross profile: Releasing the stress and boosting long-cycling and high-rate potassium ion storage, *J. Mater. Chem. A*, 2019, **7**, 25845–25852.

3 L. Zhu, Z. Li, G. Ding, L. Xie, Y. Miao and X. Cao, Review on the recent development of Li_3VO_4 as anode materials for lithium-ion batteries, *J. Mater. Sci. Technol.*, 2021, **89**, 68–87.

4 L. Zhu, Z. Wang, W. Lei, L. Xie, Ji. Li and X. Cao, ZnSe embedded in N-doped carbon nanocubes as anode materials for high-performance Li-ion batteries, *Chem. Eng. J.*, 2020, **364**, 503–513.

5 B. Wang, F. Yuan, Q. Yu, W. Li, H. Sun, L. Zhang, D. Zhang, Q. Wang, F. Lai and W. Wang, Amorphous carbon/graphite coupled polyhedral microframe with fast electronic channel and enhanced ion storage for potassium ion batteries, *Energy Storage Mater.*, 2021, **38**, 329–337.

6 F. F. Cao, J. W. Deng, S. Xin, H. X. Ji, O. G. Schmidt, L. J. Wan and Y. G. Guo, Cu–Si nanocable arrays as high-rate anode materials for lithium-ion batteries, *Adv. Mater.*, 2011, **23**, 4415–4420.

7 C. Lu, Z. Li, Z. Xia, C. Ci, J. Cai, Y. Song, L. Yu, W. Yin, S. Dou, J. Sun and Z. Liu, Confining MOF-derived SnSe nanoplatelets in nitrogen-doped graphene cages *via* direct CVD for durable sodium ion storage, *Nano Res.*, 2019, **12**, 3051–3058.

8 L. Zhang, H. Li, H. Xie, T. Chen, C. Yang and J. wang, MOF-driven ultra-small hollow Co_9S_8 nanoparticles embedded in porous carbon for lithium-ion batteries, *J. Mater. Res.*, 2018, **33**, 1496–1505.

9 X. Jiang, X. Yang, Y. Zhu, J. Shen, K. Fan and C. Li, In situ assembly of graphene sheets-supported SnS_2 nanoplates into 3D macroporous aerogels for high-performance lithium-ion batteries, *J. Power Sources*, 2013, **237**, 178–186.

10 C. He, S. Wu, N. Zhao, C. Shi, E. Liu and J. Li, Carbon encapsulated Fe_3O_4 nanoparticles as a high-rate lithium ion battery anode material, *ACS Nano*, 2013, **7**, 4459–4469.

11 Y. Wu, Y. Yi, Z. Sun, H. Sun, T. Guo, M. Zhang, L. Cui, K. Jiang, Y. Peng and J. Sun, Bimetallic Fe-Ni phosphide carved nanoframes toward efficient overall water splitting and potassium-ion storage, *Chem. Eng. J.*, 2020, **390**, 124515.

12 Z. Li, W. Li, H. Xue, W. Kang, X. Yang, M. Sun, Y. Tang and C. S. Lee, Facile fabrication and electrochemical properties of high-quality reduced graphene oxide/cobalt sulfide composite as anode material for lithium-ion batteries, *RSC Adv.*, 2014, **4**, 37180–37186.

13 H. Geng, J. Yang, Z. Dai, Y. Zhang, Y. Zheng, H. Yu, H. Wang, Z. Luo, Y. Guo, Y. Zhang, H. Fan, X. Wu, J. Zheng, Y. Yang, Q. Yan and H. Gu, Co_9S_8/MoS_2 yolk–shell spheres for advanced Li/Na storage, *Small*, 2017, **13**, 1603490.

14 Q. Zhou, L. Liu, Z. Huang, L. Yi, X. Wang and G. Cao, Co_3S_4@polyaniline nanotubes as high-performance anode materials for sodium ion batteries, *J. Mater. Chem. A*, 2016, **4**, 5505–5516.

15 H. Sun, J. Wanga, W. Li, F. Yuan, Q. Wang, D. Zhang, B. Wang and Y. A. Wu, Spanish-dagger shaped CoP blooms decorated N-doped carbon branch anode for high-performance lithium and sodium storage, *Electrochim. Acta*, 2021, **388**, 138628.

16 S. Zhang, D. Li, S. Chen, X. Yang, X. Zhao, Q. Zhao, S. Komarneni and D. Yang, Highly stable supercapacitors with MOF-derived Co_9S_8/carbon electrodes for high rate electrochemical energy storage, *J. Mater. Chem. A*, 2017, **5**, 12453–12461.

17 S. Ko, J. I. Lee, H. S. Yang, S. Park and U. Jeong, Mesoporous CuO particles threaded with CNTs for high-performance lithium-ion battery anodes, *Adv. Mater.*, 2012, **24**, 4451–4456.

18 J. S. Chen and X. W. Lou, SnO_2-based nanomaterials: Synthesis and application in lithium-ion batteries, *Small*, 2013, **9**, 1877–1893.

19 X. Y. Yu, L. Yu and X. W. D. Lou, Metal sulfide hollow nanostructures for electrochemical energy storage, *Adv. Energy Mater.*, 2016, **6**, 1501333.

20 C. Dong, L. Guo, Y. He, L. Shang, Y. Q. Qian and L. Xu, Ultrafine $Co_{1-x}S$ nanoparticles embedded in a nitrogen doped porous carbon hollow nanosphere composite as an anode for superb sodium-ion batteries and lithium-ion batteries, *Nanoscale*, 2018, **10**, 2804–2811.

21 J. Gascon, A. Corma, F. Kapteijn and F. X. L. I. Xamena, Metal organic framework catalysis: Quo vadis?, *ACS Catal.*, 2013, **4**, 361–378.

22 L. Wang, Z. Wang, L. Xie, L. Zhu and X. Cao, ZIF-67 derived N-doped Co/C nanocubes as high-performance anode materials for lithium-ion batteries, *ACS Appl. Mater. Interfaces*, 2019, **18**, 16619–16628.

23 J. Yang, F. Zhang, H. Lu, X. Hong, H. Jiang, Y. Wu and Y. Li, Hollow Zn/Co ZIF Particles Derived from Core–Shell ZIF-67@ZIF-8 as Selective Catalyst for the Semi-Hydrogenation of Acetylene, *Angew. Chem.*, 2015, **127**, 11039–11043.

24 Y. Huang, Y. Fang, X. Lu, D. Luan and X. Lou, Co_3O_4 hollow nanoparticles embedded in mesoporous walls of carbon nanoboxes for efficient lithium storage, *Angew. Chem., Int. Ed.*, 2020, **45**, 20086–20090.

25 D. K. Panchariya, R. K. Rai, E. A. Kumar and S. K. Singh, Core-shell zeolitic imidazolate frameworks for enhanced hydrogen storage, *ACS Omega*, 2018, **3**, 167–175.

26 J. Tang, R. R. Salunkhe, J. Liu, N. L. Torad, M. Imur, S. Furukawa and Y. Yamauchi, Thermal conversion of core-shell metal-organic frameworks: A new method for selectively functionalized nanoporous hybrid carbon, *J. Am. Chem. Soc.*, 2015, **137**, 1572–1580.

27 J. Qian, F. Sun and L. Qin, Hydrothermal synthesis of zeolitic imidazolate framework-67 (ZIF-67) nanocrystals, *Mater. Lett.*, 2012, **82**, 220–223.

28 S. Bhattacharyya, C. Das and T. K. Maji, MOF derived carbon based nanocomposite materials as efficient electrocatalysts for oxygen reduction and oxygen and hydrogen evolution reactions, *RSC Adv.*, 2018, **8**, 26728–26754.

29 H. Shangguana, W. Huang, C. Engelbrekt, X. Zheng, F. Shen, X. Xiao, L. Ci, P. Si and J. Zhang, Well-defined cobalt sulfide nanoparticles locked in 3D hollow nitrogen-doped carbon shells for superior lithium and sodium storage, *Energy Storage Mater.*, 2019, **18**, 114–124.

30 W. Zhou, P. Wang, C. Li, Q. Huang, J. Wang, Y. Zhu, L. Fu, Y. Chen and Y. Wu, CoS_x/C hierarchical hollow nanocages from a metal–organic framework as a positive electrode with enhancing performance for aqueous supercapacitors, *RSC Adv.*, 2019, **9**, 11253–11262.

31 C. Yuan, D. Lu, Y. An and X. Bian, A Nanocomposite of Si@C nanosphere and hollow porous Co_9S_8/C polyhedron as high-performance anode for lithium-ion battery, *ChemElectroChem*, 2020, **21**, 4423–4430.

32 Y. Tian, Y. An, C. Liu, S. Xiong, J. Feng and Y. Qian, Reversible zinc-based anodes enabled by zincophilic antimony engineered MXene for stable and dendrite-free aqueous zinc batteries, *Energy Storage Mater.*, 2021, **41**, 343–353.

33 D. Lu, C. Yuan, M. Yu, Y. Yang, C. Wang, R. Guan and X. Bian, Nanoporous composites of CoO_x quantum dots and ZIF-derived carbon as high-performance anodes for lithium-ion batteries, *ACS Omega*, 2020, **5**, 21488–21496.

34 C. L. Zhang, B. R. Lu, F. H. Cao, Z. L. Yu, H. P. Cong and S. H. Yu, Hierarchically structured Co_3O_4@carbon porous fibers derived from electrospun ZIF-67/PAN nanofibers as anodes for lithium ion batteries, *J. Mater. Chem. C*, 2018, **6**, 12962–12968.

35 B. Wang, F. Yuan, J. Wang, Q. Wang, Z. Li, W. Zhao, Y. Li, J. Feng and W. Li, Synthesis of pomegranate-structured Si/C microspheres using P123 as surfactant for high-energy lithium-ion batteries, *J. Electroanal. Chem.*, 2020, **864**, 114102.

36 K. Tang, R. J. White, X. Mu, M. M. Titirici, V. Aken and P. A. Maier, Hollow carbon nanospheres with a high rate capability for lithium-based batteries, *ChemSusChem*, 2012, **5**, 400–403.

37 B. Wang, F. Yuan, W. Li, Q. Wang, X. Ma, L. Gu, H. Sun, K. Xi, D. Zhang and W. Wang, Rational formation of solid electrolyte interface for high-rate potassium ion batteries, *Nano Energy*, 2020, **75**, 104979.

38 Z. Guo, C. Feng, G. Du, S. Wang, L. Li, X. Jiang, G. Li and S. Kim, Synthesis and characterization of cobalt-doped WS_2 nanorods for lithium battery applications, *Nanoscale Res. Lett.*, 2010, **5**, 1301–1306.

39 H. Lv, S. Qiu, G. Lu, Y. Fu, X. Li, C. Hu and J. Liu, Nanostructured antimony/carbon composite fibers as anode material for lithium-ion battery, *Electrochim. Acta*, 2015, **151**, 214–221.

40 R. Jin, J. Zhou, Y. Guan, H. Liu and G. Chen, Mesocrystal Co_9S_8 hollow sphere anodes for high performance lithium ion batteries, *J. Mater. Chem. A*, 2014, **2**, 13241–13244.

41 W. Shi, J. Zhu, X. Rui, X. Cao, C. Chen, H. Zhang, H. H. Hng and Q. Yan, Controlled synthesis of carbon-coated cobalt sulfide nanostructures in oil phase with enhanced Li storage performances, *ACS Appl. Mater. Interfaces*, 2012, **4**, 2999–3006.